Remote Sensing Letters

ISSN: 2150-704X (Print) 2150-7058 (Online) Journal homepage: www.tandfonline.com/journals/trsl20

Numerical simulation of the effect of the sea surface current gradient on the SAR radial velocity

Anis Elyouncha, Adrien C. H. Martin & Christine Gommenginger

To cite this article: Anis Elyouncha, Adrien C. H. Martin & Christine Gommenginger (2025) Numerical simulation of the effect of the sea surface current gradient on the SAR radial velocity, Remote Sensing Letters, 16:9, 970-980, DOI: 10.1080/2150704X.2025.2521066

To link to this article: https://doi.org/10.1080/2150704X.2025.2521066

Published online: 30 Jun 2025.

REMOTE SENSING LETTERS
2025, VOL. 16, NO. 9, 970–980
https://doi.org/10.1080/2150704X.2025.2521066

Taylor & Francis
Taylor & Francis Group

Numerical simulation of the effect of the sea surface current gradient on the SAR radial velocity

Anis Elyouncha [a], Adrien C. H. Martin [b,c] and Christine Gommenginger [b]

[a]Department of Marine Sciences, University of Gothenburg, Gothenburg, Sweden; [b]National Oceanography Centre (NOC), Southampton, UK; [c]NOVELTIS, Labége, France

ABSTRACT

Wave-current interactions are typically neglected when retrieving radial velocities from synthetic aperture radar (SAR) data. In this study, the impact of spatially varying currents on wind waves and swell, and on SAR-derived radial velocity, is simulated using the SWAN wave model and two semi-empirical Doppler models. Simulations were conducted for two wind speeds (5 and 10 m s^{-1}) along with two current profiles (convergent and divergent). The results indicate that the magnitude of variation in wave-induced Doppler velocity (ΔU_D) increases with the strength of the current gradient. This is primarily attributed to the increase (decrease) in significant wave height (H_s) and the decrease (increase) in peak period (T_p) under convergent (divergent) currents. Additionally, convergent currents lead to larger variations in ΔU_D. The impact of wind speed is relatively minor. When considering only the modulation of H_s, ΔU_D exceeds 0.1 m s^{-1} only in cases where the current front is 1 km wide, and this threshold is surpassed only locally. However, when both H_s and T_p modulations are taken into account, ΔU_D exceeds 0.1 m s^{-1} over approximately 10 km beyond the front. In contrast, the swell-current interaction under the conditions simulated in this study results in a negligible ΔU_D.

ARTICLE HISTORY
Received 24 September 2024
Accepted 9 June 2025

KEYWORDS
Ocean surface current; wave-current interaction; SAR; wave Doppler

1. Introduction

It is well known that spatially varying ocean surface currents affect significantly surface waves properties Bretherton, John Raymond Garrett, and James Lighthill (1968); Miles (1967). Waves are modulated by ocean currents via wave-current interaction, which changes their frequency, amplitude and direction of propagation. This has been demonstrated via numerical modelling Ardhuin et al. (2017); Bôas et al. (2020) and observations at various spatial scales Ardhuin et al. (2017). It has been found that wave-current interaction induces large spatial inhomogeneity of the wave field, resulting in variations of significant wave height and steepness of up to 30 % and enhancement of wave breaking Romero, Lenain, and Kendall Melville (2017).

CONTACT Anis Elyouncha anis.elyouncha@gu.se Department of Marine Sciences, University of Gothenburg, Box 461, Göteborg 405 30, Sweden

These current-induced variations of the wave field affect directly the quantities measured by remote sensing satellites. Synthetic aperture radar (SAR) offers the possibility to observe the sea surface current with very high spatial resolution thanks to techniques such as Doppler centroid analysis Chapron, Collard, and Ardhuin (2005); Elyouncha et al. (2019); Martin et al. (2022) and along-track interferometry, e.g., Elyouncha et al. (2021). SAR has been routinely providing valuable information on sea surface winds and waves for decades. However, extracting surface currents from SAR is still challenging due to the contribution of surface waves to the measured Doppler shift.

SAR intensity images of bright/dark quasi-linear current-induced signatures have been reported in several papers, e.g., V. Kudryavtsev et al. (2014, 2013). Under favourable conditions (moderate wind speed), the observed features in SAR images represent local ocean surface roughness anomalies resulting from the interaction of waves with spatially varying surface currents. These features are also interpreted as enhancement/suppression of wave breaking due to wave – current interaction V. Kudryavtsev et al. (2014).

This letter focuses on the impact of ocean surface current gradients on the SAR Doppler shift. This issue is relevant to all active microwave sensors, including Doppler scatterometers. While significant efforts have been made to interpret radar intensity signatures, e.g., V. Kudryavtsev et al. (2014, 2013), the effect of currents on the Doppler signature has not been investigated yet. The extent to which this phenomenon affects SAR Doppler measurements, and consequently, the radial velocity and surface current speed derived from these measurements, remains unknown in terms of both magnitude and spatial extent.

The Doppler signature of the sea surface consists of the desired total surface current leading to an effective horizontal transport, combining geostrophic and ageostrophic components and of an unwanted artefact known as Wave Doppler or Wind-wave Artefact Surface Velocity (WASV) Martin et al. (2016), which is caused by a correlation between the scatterer radar reflectivity and their motions as they are advected by the long ocean waves Elyouncha and Romeiser (2024). Theoretical or empirical Doppler models, e.g., V. Kudryavtsev et al. (2023); Mouche et al. (2012); Yurovsky et al. (2019) are commonly used to evaluate the WASV, using wind and/or wave parameters as input. The model-calculated WASV is then simply subtracted from the total measured Doppler shift Elyouncha et al. (2021); Martin et al. (2022). Typically, this WASV is calculated assuming a mean sea state and does not take into account any wave-current interaction. In this study, we evaluate the impact of wave-current interaction on the WASV in terms of amplitude and spatial extent.

2. Background

An ocean wave field develops by responding to wind forcing, and it is influenced by the current field and topography. The acquired energy is dissipated and redistributed over frequencies. Its evolution in time and space is a result of the interaction between the waves, a varying wind field, bathymetry and currents.

Waves propagating over a current are subject to a Doppler shift of their frequency. The absolute frequency ω (the radian frequency of the wave in a fixed frame of reference) is related the relative frequency σ (the radian frequency as observed in a frame of reference moving with the current) by Miles (1967) $\omega = \sigma + k \cdot U$, where k is the wavevector of the

wave and U is the current velocity. σ is given by the dispersion relation $\sigma^2 = gk\tanh(kd)$, where g is the gravity-induced acceleration, k is the wavenumber and d is the water depth.

Assuming a slowly varying current, i.e., current with length and time scales larger than the wavelength and period of the wave, and a constant depth, the rate of change of ω, k and σ are given by Bretherton, John Raymond Garrett, and James Lighthill (1968); Tolman (1990)

$$\frac{d\omega}{\partial t} = -k \cdot \frac{\partial U}{\partial t}, \frac{dk}{\partial t} = -k \cdot \frac{\partial U}{\partial x}, \frac{d\sigma}{\partial t} = -c_g k \cdot \frac{\partial U}{\partial x}$$

The first equation indicates that if the current is steady, the absolute frequency ω is conserved. The second and third equations indicate that only if the current U is nonuniform ($\frac{\partial U}{\partial x} \neq 0$), the wavenumber k and σ will vary. In other words, σ and k will adjust to current variation to conserve ω. Let us assume a current and a wave propagating in the same direction. If the current gradient is positive (accelerating current), σ and k will decrease, i.e., wave becomes longer. If the current gradient is negative (decelerating current), σ and k will increase, i.e., the wave becomes shorter.

While the wave energy E is not conserved, due the exchange of energy between the waves and the current, the wave action E/σ is conserved Bretherton, John Raymond Garrett, and James Lighthill (1968); Miles (1967). Thus, an increase (decrease) in σ, due to a spatial current gradient, implies an increase (decrease) in wave energy and consequently in wave amplitude, since the energy is proportional to wave amplitude squared $E = \frac{1}{2}\rho g a^2$, where ρ is the water density and a is the wave amplitude. Therefore, if the current gradient is positive (negative), the wave amplitude decreases (increases). Moreover, since the wavenumber and amplitude change in the same direction, the wave steepness will decrease (increase) with accelerating (decelerating) current.

The development and evolution of a wave field, including the wave-current interaction, is fully described by the spectral wave action balance equation. In 1D, with the current and wave propagating in the xx-direction and assuming a steady current and wind fields, the wave action balance equation reads

$$\frac{\partial (C_g + U)N}{\partial x} = \frac{S_{in} + S_{ds} + S_{nl}}{\sigma} \tag{1}$$

where $N = E/\sigma$ is the wave action density spectrum. $C_g (= \partial\sigma/\partial k)$ is the group velocity. S_{in} is a source term representing the input by wind, S_{ds} is a sink term representing the dissipation, which is composed of three terms: whitecapping S_{wc}, bottom friction S_{bf} and depth-induced breaking S_{br} ($S_{ds} = S_{wc} + S_{bf} + S_{br}$); and S_{nl} is the nonlinear wave–wave interaction, which is composed of triads and quadruplets ($S_{nl} = S_{tr} + S_{qd}$). In deep water, the four-wave interactions (quadruplets) are much more important than the three-wave interactions (triads) (Holthuijsen 2007). Thus, in deep water, the right-hand side in Equation (1) reduces to $[S_{in} + S_{wc} + S_{br} + S_{qd}]/\sigma$.

Numerical wave models, such as SWAN, WAM and WWIII, solve the wave action balance equation numerically to determine the evolution of the action density in space and time. Equation (1) is a partial differential equation. Its solution requires an initial condition and a boundary condition. Wave models offer several options for the initial wave spectrum such as Pierson-Moskowitz (PM) Pierson and Moskowitz (1964) and JONSWAP Hasselmann et al. (1973) models.

3. Method

This study combines numerical wave modelling with semi-empirical electromagnetic models. The SWAN wave model Booij, Ris, and Holthuijsen (1999); Holthuijsen (2007) is used to simulate current-induced changes in wave height and period, while the semi-empirical wave Doppler electromagnetic models, KaDOP Yurovsky et al. (2019) and DPDop Fan et al. (2023); V. Kudryavtsev et al. (2023), are employed to simulate the corresponding changes in SAR Doppler shift.

3.1. Model setup

In this study, the SWAN model is used to solve the spectral action balance equation. The domain grid is Cartesian one-dimensional extending from $x = 0$ to $x = 200$ km with a constant grid spacing $\Delta x = 1$ km and a constant depth $d = 1000$ m. The selected Δx is similar to the spatial sampling of existing Sentinel-1 ocean products Engen and Johnsen (2015) and SEASTAR mission concept Gommenginger, Christine, Bertrand Chapron, Andy Hogg, Christian Buckingham, and Fox-Kemper (2019), and comparable (though coarser) to the future Doppler scatterometer mission ODYSEA (5 km) Rodríguez et al. (2019).

For wind waves, the ocean is forced by the current-relative wind. The direction of propagation of the waves is parallel to the current. The refraction effect is negligible and thus not discussed here. The background wave spectrum is JONSWAP with the directional distribution ($\cos^2(\theta - \theta_{peak})$), where θ and θ_{peak} are the wave direction and wave direction at the peak of the spectrum. The wind direction is set to 270 ° (coming from the west) with a 200 km fetch. A combination of two different front widths ($L = 1$ km and $L = 3$ km) and two wind speeds ($U_{10} = 5$ and $U_{10} = 10$ m s^{-1}). Two scenarios are simulated, waves propagating over a convergent current and waves propagating over a divergent current. The current is zero from 0 to 100 km and negative (positive) for the convergent (divergent) from 100 km to 200 km with magnitude 1 m s^{-1}. A total of eight simulations were performed. In addition, a swell of 2 m significant wave height and 12 s period coming from the west and propagating parallel to the current is simulated. These swell parameters are representative of the global average swell. The swell is simulated using a narrow Gaussian spectrum of 5 ° width.

Given the deep water conditions, bottom friction is negligible and is thus not activated. Given also the large depth, the depth-induced breaking, i.e., shoaling, is also neglected. As mentioned above, in deep and intermediate water, four-wave interactions (quadruplets) are more important than triads Holthuijsen (2007). Thus, the triads are neglected. Finally, the default parameterizations are applied for all other settings including wind generation, white-capping and quadruplets.

For each scenario, two model runs are conducted: a run without current (control run, $U = 0$) and a run with current (convergent or divergent). The model is run in stationary mode, i.e., the wind and current are time independent.

3.2. Wave-induced Doppler estimation

The semi-empirical wave Doppler simulators (KaDOP and DPDop) are used to estimate the wave-induced Doppler (WASV). These models take as inputs: the

radar wavelength λ_r, incidence angle θ, wind speed u_{10}, relative wind direction φ_{10}, significant wave height H_s and peak frequency (σ_p) for wind sea and swell and returns as output the Doppler velocity U_D, i.e., the Doppler frequency shift (in Hz) converted to radial velocity (in m s^{-1}). For this study, the model is run for Ku-band ($\sim$13.6 GHz, $\lambda_r = 0.022$ m) at $\theta = 30^\circ$. The two quantities (H_s and σ_p) are affected by the wave-current interaction which affects the estimated wave Doppler velocity.

The objective of this section is to quantify the effect of wave-current interaction on the wind wave and swell. To evaluate the effect of wave-current interaction on the wind waves, the swell effect is deactivated in the KaDOP model, i.e., the β_{sw} (see Eq. 16 in Yurovsky et al. (2019)) is set to zero, to get only the wind-wave contribution. To evaluate the swell effect, the wind-wave effect is deactivated in the model, i.e., the β_{ws} (see Eq. 16 in Yurovsky et al. (2019)) is set to zero, to get only the swell contribution. The DPDop model does not distinguish between wind waves and swell.

The significant wave height H_s is estimated from the zero-moment of the wavenumber spectrum as follows $H_s = 4\sqrt{m_0}$, where $m_n = \int^{k^n} E(k)\mathrm{d}k$. The peak wave (radian) frequency is also estimated from the wave spectrum using the zero and second moments as follows $\sigma_p = 2\pi/\sqrt{m_0/m_2}$. The peak period T_p is calculated using the dispersion relation. Alternatively, T_p can me estimated by detecting the peak of the spectrum and finding the corresponding wave number (k_p).

First, the background (without current) wave spectrum (E) and the modulated wave spectrum ($\tilde{E}$) are calculated by solving the wave action balance equation using SWAN wave model. Second, the background wave parameters H_s and σ_p and the perturbed wave parameters $\tilde{H}_s$ and $\tilde{\sigma}_p$ are estimated from the background E and the perturbed spectra $\tilde{E}$, respectively, using Eqs. 7–9. Third, the Doppler model (DOP) is called with these parameters to estimate the background $U_D = \mathrm{DOP}(\theta, u_{10}, \varphi_{10}, H_s, \sigma_p)$. The modulated $\tilde{U}_D$ is calculated for two cases, by taking into account the H_s modulation only, i.e., $U_D = \mathrm{DOP}\left(\theta, u_{10}, \varphi_{10}, \tilde{H}_s, \sigma_p\right)$ and by taking into account both the H_s and σ_p modulations $U_D = \mathrm{DOP}\left(\theta, u_{10}, \varphi_{10}, \tilde{H}_s, \tilde{\sigma}_p\right)$.

4. Results and discussion

For wind waves, only the results obtained with $U_{10} = 10$ m s^{-1} and $L = 1$ km are shown here. However, numerical results are reported for all runs in Table 1. As shown later, the swell effect is very small to negligible. Hence, only the worst-case swell results, i.e., with $L = 1$ km, are reported.

Figure 1(b) illustrates the effect of current variation on the omnidirectional wind wave spectrum. It is worth noting that the variation is not uniform over frequency. The intermediate waves with frequencies between 0.2 and 0.3 hz or wavelength between approximately 20 and 50 m are the most affected, while longer and shorter waves are less or negligibly affected. Also, the convergent current generates larger modulations than the divergent current. Though the effect of divergent current is smaller than the convergent current, the difference between the non-modulated (black curve) and modulated (blue dashed curve) wave spectrum is clearly visible. The convergent current gradient

Table 1. Maximum variation of significant wave height, steepness and wave-induced Doppler velocity for wind waves and swell. ΔU_D is calculated by taking into account ΔH_s only and both ΔH_s and ΔT_p. Swell-related results are only shown for the highest divergence. $\Delta\varepsilon$ is the change in steepness, where $\varepsilon = ka$.

Front width (km)	Divergence 1e-3(10^{-3}s^{-1})	u_{10} (m s^{-1})	ΔH_s (cm)	$\Delta\varepsilon$	ΔU_D (m s^{-1}) (w/with H_s)	ΔU_D (m s^{-1}) (w/with H_s &and T_p)
Convergent current - wind waves						
3	−0.08	5	2.57	0.0197	0.06	0.16
3	−0.08	10	10.76	0.0167	0.08	0.15
1	−0.19	5	4.41	0.026	0.10	0.23
1	−0.19	10	13.83	0.021	0.11	0.20
Convergent current - swell						
1	−0.19	-	25.24	0.007	0.007	0.013
Divergent current - wind waves						
3	0.08	5	−2.40	0.016	−0.049	−0.116
3	0.08	10	−5.79	0.015	−0.044	−0.119
1	0.19	5	−3.76	0.019	−0.076	−0.138
1	0.19	10	−8.02	0.017	−0.060	−0.136
Divergent current - swell						
1	0.19	-	−18.57	0.005	−0.004	−0.008

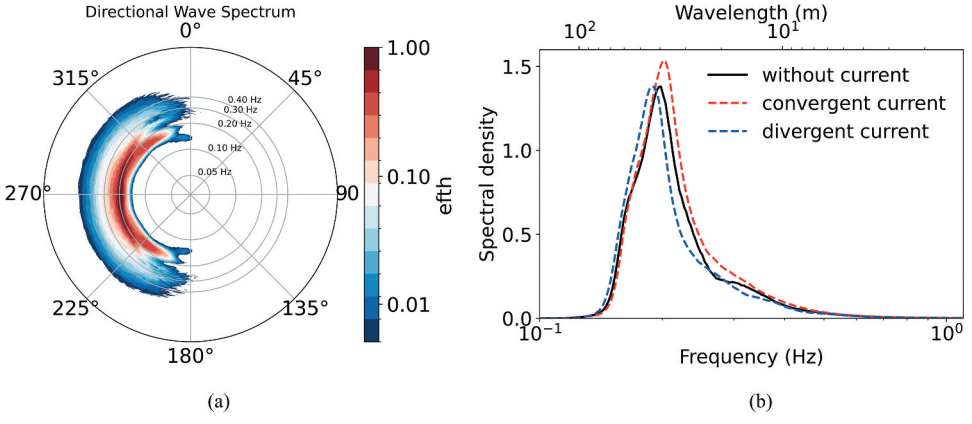

Figure 1. Effect of current gradient on the wave spectrum. Left panel. (a): Directional wave spectrum (U_{10} = 10 m s^{-1}, $\varphi_{10} = 270°$), efth: directional variance spectral density in m^2 Hz^{-1} deg^{-1}, right panel(b): spectrum modulation (U_{10} = 10 m s^{-1}, front width 1 km).

compresses the waves (shorter wavelength, higher frequency) and the divergent current dilates the waves (longer wavelength and lower frequency). Hence, the peak wavelength/frequency shift.

Figure 2 illustrates the effect of current variation (bottom row), over the 200 km fetch, on T_p (middle row) and H_s (top row) for a convergent/decelerating current (left panel, panel a) and divergent/accelerating current (right panel, panel b). The H_s increases from zero to about 1.5 m where it reaches fully developed sea conditions. Away from the convergence and divergence zone, where the current gradient is zero, the curves with (dashed red) and without current (blue) are virtually identical, i.e., no modulation. Around the maximum convergence, H_s increases and T_p decreases while around the maximum

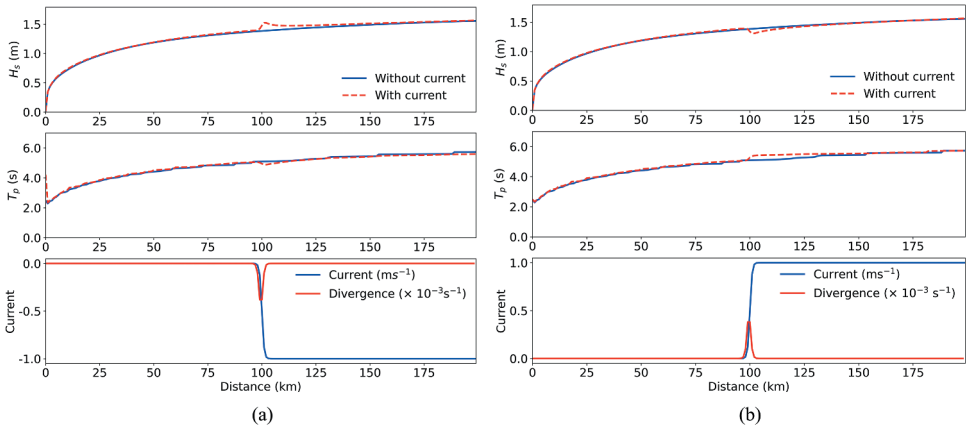

Figure 2. Effect of current gradient on H_s and T_p. Left panel. (a): convergent current - U_{10} = 10 m s^{-1}, L = 1 km, right panel. (b): divergent current, U_{10} = 10 m s^{-1}, L = 1 km. Top row: H_s variation, middle row: T_p variation, bottom row: current variation and divergence.

divergence H_s decreases and T_p increases. The perturbation is local and attenuates gradually to return to equilibrium. This return to equilibrium (relaxation) takes a few kilometers. Similar effect is observed in the swell case (not shown), with a comparable change in H_s but a smaller change in T_p. Also, the return to equilibrium is much slower than for the wind wave case.

Figure 3 is a zoom of 30 km on each side of the front centred on x = 100 km showing the difference of H_s and U_D in the presence of current gradient and without current. It can be readily noticed that up to 14 cm H_s change is reached. This change is larger in convergent (opposing) current than divergent (following) current. If only H_s is taken into account for the WASV estimate, the calculated U_D modulation reaches 10 cm s^{-1} only very locally and only for the convergent current. However, when taking into account both H_s and T_p modulations, i.e., taking into account slope modulation, the calculated U_D modulation exceeds 10 cm s^{-1} over several kilometres. For the swell case (not shown), the calculated U_D modulation is an order of magnitude smaller than for the wind wave case. The two Doppler models agree relatively well on the induced Doppler modulation, with KaDOP giving a slightly higher modulation.

In summary, a series of eight simulations were conducted, combining two different front widths (1 km and 3 km), corresponding to two different divergence values (0.08 and 0.19 $\times 10^{-3}$ s^{-1}), and two wind speeds (5 and 10 m s^{-1}). Additionally, two simulations were run for swell conditions with a front width of 1 km. Table 1 summarizes the results of these simulations, showing the maximum variations in significant wave height (ΔH_s) and Doppler velocity (ΔU_D) at x = 100 km. As expected, the magnitude of ΔH_s and ΔU_D increases with the strength of the current divergence. While wind speed has a noticeable effect on ΔH_s, its impact on ΔU_D is minimal and even slightly decreases with higher wind speeds. This might be explained as follows: It is known that U_D increases with wind speed, basically because stronger wind generates steeper waves with larger orbital velocities. The increase of U_D with wind speed is nonlinear, becoming slower at high wind. Thus, the change in U_D, i.e., ΔU_D, is smaller at high wind than at low wind. This

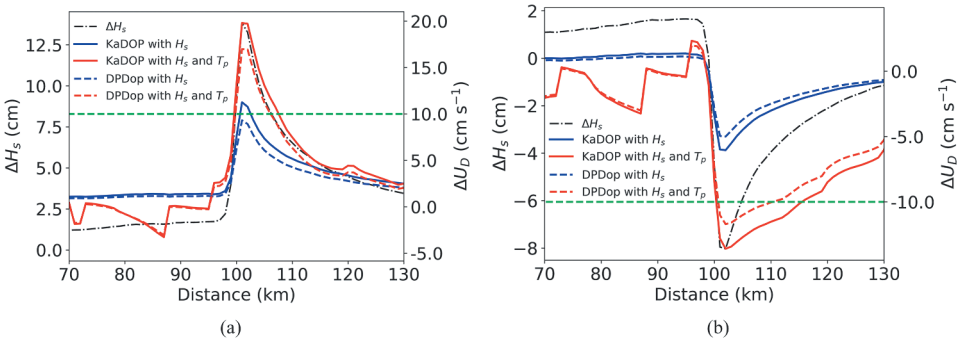

Figure 3. Effect of current gradient on SAR radial velocity. Left panel. (a): convergent current, right panel. (b): divergent current. U_{10} = 10 m s^{-1}, L = 1 km. Blue curve: U_D bias by taking into account H_s modulation only. Red curve: U_D bias by taking into account H_s and T_p modulations. The solid curves correspond to KaDOP and the dashed curves to DPDop. The horizontal green dashed line indicates a hypothetical 0.1 m s^{-1} accuracy target. Only a section of 60 km centered at the front is shown.

is mainly due to the tilt and hydrodynamic modulation transfer functions, which are the main components of the wave Doppler model, that decrease with increasing wind speed.

It is also observed that a convergent current, i.e., when waves propagate against the current, results in larger ΔH_s and ΔU_D than a divergent current (see Figure 3). With a current gradient of 1 m s^{-1}, the wave bias exceeds 0.1 m s^{-1} in only two cases, when the current is convergent with a 1 km wide front, resulting in a divergence of 0.19×10^{-3} s^{-1}, for both wind speeds tested (5 and 10 m s^{-1}). In these scenarios, if we set a 0.1 m s^{-1} accuracy threshold, this limit is exceeded over approximately 3 km. When the modulation of the wave period T_p, in addition to H_s, is considered in the estimation of U_D, the 0.1 m s^{-1} threshold is exceeded over a longer distance (~10 km) across all simulations. As shown in Table 1, the ΔU_D is negligible in the case of the simulated swell. This is primarily due to its very low steepness ($\varepsilon = ka$), where k is the wavenumber and a is the wave amplitude, in contrast to the steeper wind waves. This is consistent with theoretical predictions. The long wave-induced Doppler velocity (U_D) is the dominant contribution to the SAR wave Doppler model. The formulation of these terms, e.g., Eq. 6 in Yurovsky et al. (2019) or Eq. 12 and 13 in Fan et al. (2023), indicates that they are proportional to ωka^2. That is, at a given incidence angle, wind speed and direction, U_D increases with the wave frequency, wave number and amplitude squared. In other words, the steeper high-frequency wind waves will induce larger U_D than the shallower low-frequency swell.

5. Conclusion

The spectral density increases in regions of current convergence and decreases in regions of divergence, with intermediate waves (wavelengths on the order of 10 metres) being particularly sensitive to these changes. The magnitude of variation in significant wave height (H_s) and Doppler shift (U_D) increases with the strength of the current gradient. Wind speed has a smaller impact on U_D compared to the influence of the current gradient. Notably, convergent currents cause larger variations in ΔH_s and ΔU_D than divergent currents. Including the period variation ΔT_p results in higher ΔU_D

compared to considering H_s alone. If an accuracy threshold of 10 cm s^{-1} is set, then in the extreme case of a 1 m s^{-1} current gradient over 1 km, this threshold is exceeded for approximately 10 km beyond the front in the down-wave direction. The current-gradient modulation of the swell yields a ΔU_D that is an order of magnitude smaller than that caused by wind-waves, with the simulated ΔU_D for swell not exceeding 1.3 cm s^{-1}.

This study is based on a one-dimensional simulation, and the results and conclusions are specific to this configuration. However, wind-wave propagation parallel to the current gradient (perpendicular to the front) likely represents the worst-case scenario for wave amplitude modulation and the resulting Doppler velocity. The impact of current gradient and relative wind direction will be assessed in further study. Additionally, a deep water approximation was assumed, which neglects bottom-induced dissipation, refraction and shoaling effects. Since many SAR images are acquired in coastal areas, these effects in shallow waters with varying depths need to be further investigated.

Disclosure statement

No potential conflict of interest was reported by the author(s).

Funding

This work was funded by the Swedish National Space Agency (SNSA) contract Dnr 2023-00178 and the European Space Agency (ESA) in the framework of Earth Explorer 11 Phase 0 Science and Requirement Consolidation Study (SciReC-SEASTAR, ESA EXPRO RFP/3-17308/21/NL/FF/ab).

ORCID

Anis Elyouncha http://orcid.org/0000-0002-3586-7988

References

Ardhuin, F., S. T. Gille, D. Menemenlis, C. B. Rocha, N. Rascle, B. Chapron, J. Gula, and J. Molemaker. 2017. "Small-Scale Open Ocean Currents Have Large Effects on Wind Wave Heights." *Journal of Geophysical Research Oceans* 122 (6): 4500–4517. https://doi.org/10.1002/2016JC012413.

Bôas, V., B. Ana, D. C. Bruce, R. M. Matthew, and T. G. Sarah. 2020. "Wave–Current Interactions at Meso- and Submesoscales: Insights from Idealized Numerical Simulations." *Journal of Physical Oceanography* 50 (12): 3483–3500. https://doi.org/10.1175/JPO-D-20-0151.1.

Booij, N., R. C. Ris, and L. H. Holthuijsen. 1999. "A Third-Generation Wave Model for Coastal Regions: 1. Model Description and Validation." *Journal of Geophysical Research Oceans* 104 (C4): 7649–7666. https://doi.org/10.1029/98JC02622.

Bretherton, F. P., C. John Raymond Garrett, and M. James Lighthill. 1968. "Wavetrains in Inhomogeneous Moving Media." *Proceedings of the Royal Society of London Series A: Mathematical and Physical Sciences* 302 (1471): 529–554. https://doi.org/10.1098/rspa.1968.0034.

Chapron, B., F. Collard, and F. Ardhuin. 2005. "Direct Measurements of Ocean Surface Velocity from Space: Interpretation and Validation." *Journal of Geophysical Research Oceans* 110 (C7). https://doi.org/10.1029/2004JC002809.

Elyouncha, A., L. E. B. Eriksson, G. Bröstrom, L. Axell, and L. H. M. Ulander. 2021. "Joint Retrieval of Ocean Surface Wind and Current Vectors from Satellite SAR Data Using a Bayesian Inversion Method." *Remote Sensing of Environment* 260:112455. https://doi.org/10.1016/j.rse.2021.112455.

Elyouncha, A., E. B. Leif, H. Johnsen, and L. M. H. Ulander. 2019. "Using Sentinel-1 Ocean Data for Mapping Sea Surface Currents Along the Southern Norwegian Coast." *IGARSS 2019 - 2019 IEEE International Geoscience and Remote Sensing Symposium*, Yokohama, Japan, 8058–8061.

Elyouncha, A., and R. Romeiser. 2024. "On the Correlation Between the SAR Backscatter Modulation and Surface Waves Orbital Velocity." *IEEE Journal of Selected Topics in Applied Earth Observations and Remote Sensing* 17:13908–13924. https://doi.org/10.1109/JSTARS.2024.3438437.

Engen, G., and H. Johnsen. 2015. Sentinel-1 Doppler and Ocean Radial Velocity (Rvl) Algorithm Definition. *Technical Report*. ESA.

Fan, S., B. Zhang, A. Moiseev, V. Kudryavtsev, J. A. Johannessen, and B. Chapron. 2023. "On the Use of Dual co-Polarized Radar Data to Derive a Sea Surface Doppler Model—Part 2: Simulation and Validation." *IEEE Transactions on Geoscience and Remote Sensing* 61:1–9. https://doi.org/10.1109/TGRS.2023.3246771.

Gommenginger, C. B. Chapron, A. Hogg, C. Buckingham, and B. Fox-Kemper. 2019. "SEASTAR: A Mission to Study Ocean Submesoscale Dynamics and small-Scale atmosphere-Ocean Processes in Coastal, Shelf and Polar Seas." *Frontiers in Marine Science* 6. https://doi.org/10.3389/fmars.2019.00457.

Hasselmann, K., T. P. Barnett, E. Bouws, H. Carlson, D. E. Cartwright, K. Enke, J. A. Ewing, et al. 1973. "Measurements of Wind-Wave Growth and Swell Decay During the Joint North Sea Wave Project (JONSWAP)." *Ergnzungsheft zur Deutschen Hydrographischen Zeitschrift Reihe* 8 (12): 95.

Holthuijsen, L. H. 2007. *Waves in Oceanic and Coastal Waters*. 1st ed. Vol. 9780521860284. Cambridge, UK: Cambridge University Press.

Kudryavtsev, V., S. Fan, B. Zhang, B. Chapron, J. A. Johannessen, and A. Moiseev. 2023. "On the Use of Dual Co-Polarized Radar Data to Derive a Sea Surface Doppler Model—Part 1: Approach." *IEEE Transactions on Geoscience and Remote Sensing* 61:1–13. https://doi.org/10.1109/TGRS.2023.3235829.

Kudryavtsev, V., I. Kozlov, B. Chapron, and J. A. Johannessen. 2014. "Quad-Polarization SAR Features of Ocean Currents." *Journal of Geophysical Research Oceans* 119 (9): 6046–6065. https://doi.org/10.1002/2014JC010173.

Kudryavtsev, V. N., B. Chapron, A. G. Myasoedov, F. Collard, and J. A. Johannessen. 2013. "On Dual co-Polarized SAR Measurements of the Ocean Surface." *IEEE Geoscience and Remote Sensing Letters* 10 (4): 761–765. https://doi.org/10.1109/LGRS.2012.2222341.

Martin, A. C. H., C. Gommenginger, J. Marquez, S. Doody, V. Navarro, and C. Buck. 2016. "Wind-Wave-Induced Velocity in ATI SAR Ocean Surface Currents: First Experimental Evidence from an Airborne Campaign." *Journal of Geophysical Research Oceans* 121 (3): 1640–1653. https://doi.org/10.1002/2015JC011459.

Martin, A. C. H., C. P. Gommenginger, B. Jacob, and J. Staneva. 2022. "First Multi-Year Assessment of Sentinel-1 Radial Velocity Products Using HF Radar Currents in a Coastal Environment." *Remote Sensing of Environment* 268:112758. https://doi.org/10.1016/j.rse.2021.112758.

Miles, J. W. 1967. "The Dynamics of the Upper Ocean. By 0. M. PHILLIPS. Cambridge Uni-Versity Press." *Journal of Fluid Mechanics* 29 (4): 822–825. https://doi.org/10.1017/S0022112067211193.

Mouche, A. A., F. Collard, B. Chapron, K.-F. Dagestad, G. Guitton, J. A. Johannessen, V. Kerbaol, and M. Wergeland Hansen. 2012. "On the Use of Doppler Shift for Sea Surface Wind Retrieval from SAR." *IEEE Transactions on Geoscience and Remote Sensing* 50 (7): 2901–2909. https://doi.org/10.1109/TGRS.2011.2174998.

Pierson, W. J., Jr., and L. Moskowitz. 1964. "A Proposed Spectral Form for Fully Developed Wind Seas Based on the Similarity Theory of S. A. Kitaigorodskii." *Journal of Geophysical Research* 69 (24): 5181–5190. https://doi.org/10.1029/JZ069i024p05181.

Rodríguez, E., M. Bourassa, J. T. F. Dudley Chelton, D. Long, D. Perkovic-Martin, R. Samelson, and R. Samelson. 2019. "The Winds and Currents Mission Concept." *Frontiers in Marine Science* 6:6. https://doi.org/10.3389/fmars.2019.00438.

Romero, L., L. Lenain, and W. Kendall Melville. 2017. "Observations of Surface wave–Current Interaction." *Journal of Physical Oceanography* 47 (3): 615–632. https://doi.org/10.1175/JPO-D-16-0108.1.

Tolman, H. L. 1990. "The Influence of Unsteady Depths and Currents of Tides on wind-Wave Propagation in Shelf Seas." *Journal of Physical Oceanography* 20 (8): 1166–1174. https://doi.org/10.1175/1520-0485(1990)020<1166:TIOUDA>2.0.CO;2.

Yurovsky, Y., V. Kudryavtsev, S. Grodsky, and B. Chapron. 2019. "Sea Surface Ka-Band Doppler Measurements: Analysis and Model Development." *Remote Sensing* 11 (7): 839. https://doi.org/10.3390/rs11070839.